

Article

Design of an Axial-Type Magnetic Gear with Auxiliary Flux-Enhancing Structure

Fang Li , Hang Zhao * and Xiangdong Su

Robotics and Autonomous Systems Thrust, The Hong Kong University of Science and Technology (Guangzhou), Guangzhou 511453, China; fli078@connect.hkust-gz.edu.cn (F.L.); xsu847@connect.hkust-gz.edu.cn (X.S.)

* Correspondence: hangzhao@hkust-gz.edu.cn

Abstract: In this paper, a new axial-type magnetic gear with an auxiliary flux-enhancing structure (AFS-AMG) is proposed. Compared to conventional AMGs, it has a higher torque density and higher permanent magnet (PM) utilization factor. Firstly, the design rules and operating principles of the proposed AFS-AMG are elaborated. Then, the mapping relation between the radial-type magnetic gears (RMGs) and AMGs are elucidated. Compared to its counterparts in RMGs, the AFS-AMG achieves a small size. Then, the geometrical parameters of the AFS-AMG are optimized to obtain better electromagnetic performance, where the torque density per volume and per PM volume is adopted as the evaluation standard. Finally, three different AMG topologies are constructed in finite element analysis (FEA) software for comparison. It is proven that the AFS-AMG has the largest torque density per volume and per PM volume.

Keywords: axial magnetic gear; permanent-magnet machine; flux-enhancing effect; mapping relation; parameter optimization

1. Introduction

The mechanical gearbox is the cornerstone of variable-speed transmission systems, playing a pivotal role in aligning the torque and rotational velocity between the prime mover and the driven load. Its widespread adoption is attributed to its exceptional torque density and versatile gear ratios. However, the reliance on physical contact for power transmission in mechanical gears introduces significant tribological challenges. These challenges manifest as elevated costs associated with lubrication, cooling, and maintenance [1]. Empirical evidence underscores the fact that tooth abrasion critically undermines the reliability of mechanical gears, often emerging as a primary cause of system failures [2]. This vulnerability significantly restricts their application in industries such as food, pharmaceuticals, and chemicals, where the operational environment demands higher standards of cleanliness and system integrity. In situations where a clear separation between power input and output is required, mechanical gears may not meet these strict requirements.

Magnetic gears (MGs) are emerging as superior alternatives to traditional mechanical gearboxes, offering a host of benefits that include higher efficiency, reduced noise, and intrinsic self-protection features [3–5]. These advantages stem from MGs' ability to inherently provide overload protection through the physical separation of input and output rotors, a critical feature that significantly enhances transmission reliability [6]. Unlike mechanical gears, which rely on the direct meshing of teeth on the master and slave wheels for motion and power transmission, MGs utilize the coupling of magnetic fields between permanent magnets affixed to these wheels, a principle that is also finding applications in the design of electric motors, such as permanent-magnet field-modulation machines [7,8]. The initial phase of MG research focused on developing magnetic gear topologies by drawing parallels with the traditional designs of mechanical gears. This foundational work has led to the development of a diverse array of MG types over the past two decades. Classifying MGs by



Citation: Li, F.; Zhao, H.; Su, X. Design of an Axial-Type Magnetic Gear with Auxiliary Flux-Enhancing Structure. *Energies* **2024**, *17*, 2207. <https://doi.org/10.3390/en17092207>

Academic Editor: Frédéric Dubas

Received: 1 April 2024

Revised: 29 April 2024

Accepted: 30 April 2024

Published: 3 May 2024



Copyright: © 2024 by the authors. Licensee MDPI, Basel, Switzerland. This article is an open access article distributed under the terms and conditions of the Creative Commons Attribution (CC BY) license (<https://creativecommons.org/licenses/by/4.0/>).

their operating principles reveals a variety of types, including coaxial permanent-magnet (PM) coaxial MGs, reluctance MGs [9], cycloidal MGs [10], and planetary MGs [11]. When categorized by structural characteristics, the range expands to radial-type magnetic gears (RMGs), axial-type magnetic gears (AMGs), linear MGs [12], and tubular MGs [13]. Notably, RMGs and AMGs have attracted significant research interest for their potential to directly replace mechanical gearboxes in practical engineering applications. While RMGs are celebrated for their adaptability, certain applications may find them less suitable due to strict spatial constraints. In these instances, AMGs present an advantageous alternative, boasting higher torque density and a reduced axial length compared to RMGs [14]. The distinction between axial magnetic gears (AMGs) and radial magnetic gears (RMGs) is primarily rooted in the orientation of the permanent-magnet magnetization and the nature of their coupling surfaces. Specifically, RMGs feature magnets that are magnetized in the radial direction and utilize the radial outer circular surface for coupling. Conversely, AMGs employ an axial magnetization direction, with coupling occurring at the axial outer end surface. This fundamental difference renders AMGs particularly advantageous in applications where weight reduction is paramount, such as in aerospace technologies [15].

The historical development of AMGs was marked by a significant milestone in 1987 when Tsurumoto K. and Kikuchi S. introduced an axial magnetic gear with an involute-shaped permanent magnet, arranged in a circular pattern on a base disc, achieving a 3:1 gear ratio using SmCo₅ permanent magnets. This design was revolutionary in that it transitioned the coupling region from a radial to an axial cross-section [16], subsequently undergoing further optimizations by Tsurumoto K. [17,18]. The application of axial magnetic gears, particularly in centrifugal equipment, as investigated by Klaui [19] and Meisberger [20], has demonstrated the potential to achieve high torque densities through experimental testing. Innovations aimed at enhancing torque density have included the development of a flux-focusing axial magnetic gear, although this design was challenged by the issue of flux leakage [21,22]. An alternative approach involved employing a Halbach array to augment torque density [23]. Afsari's introduction of a magneto-resistive linkage-type axial magnetic gear presented a design that not only reduced the number of required permanent magnets but also aimed to enhance gear reliability [24]. Despite these advancements, the design faced limitations in significantly boosting gear torque and exhibited magnetic leakage in slower-rotating rotors. Furthermore, the performance evaluation of AMGs necessitates the construction of complex three-dimensional models, a process that is notably time-consuming and has, thus, limited the proliferation of research and development in this area [21,25]. The axial-direction force exerted by AMGs also poses substantial challenges to their fabrication, complicating the design process further. Another overarching concern for both types of magnetic gears is the extensive reliance on permanent magnets (PMs), which considerably inflates manufacturing costs due to the materials used.

In addressing the limitations identified in existing axial magnetic gear (AMG) designs—namely, the insufficient improvement in torque density and the consequential cost implications stemming from the extensive use of permanent magnets (PMs)—this paper introduces an innovative approach. We propose the integration of an iron-made flux-enhancing plate to the exterior of AMGs, a novel addition designed to significantly elevate the output torque. This innovative concept is meticulously analyzed through the examination of flux path variations before and after the implementation of the auxiliary flux-enhancing plane, elucidating the underlying principle of flux enhancement.

Subsequently, the performance metrics of three distinct AMG configurations are rigorously compared to demonstrate the superiority of our proposed structure. This comparison not only showcases the enhanced torque density achieved through our design but also highlights an unprecedented improvement in the PM utilization factor. By ingeniously augmenting the magnetic flux efficiency within the gear system, our approach effectively mitigates the challenges associated with high PM usage, thereby addressing both the performance and cost-efficiency concerns.

2. Structure Configuration

2.1. Design Rules and Operating Principle

The proposed auxiliary flux-enhancing structural axial-type magnetic gear (AFS-AMG) contains four planes, and its structure is depicted in Figure 1.

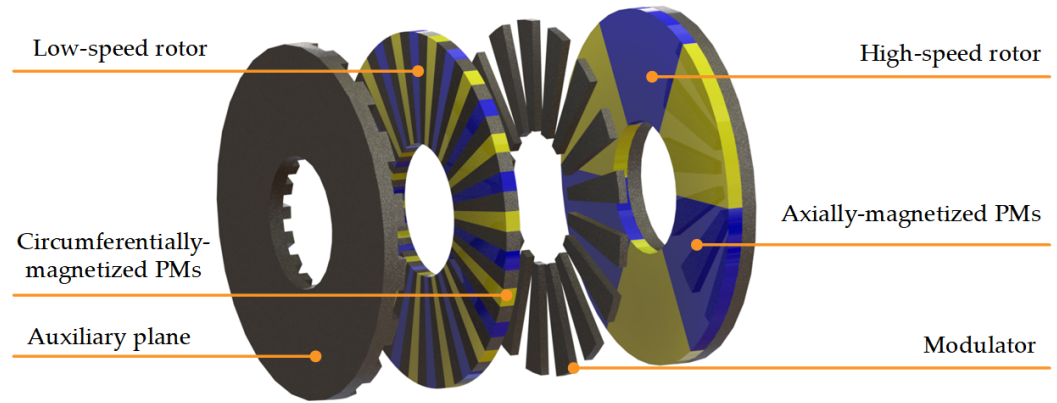


Figure 1. Exploded view of the proposed AFS-AMG.

The two rotors have surface-mounted PMs on them, and the one with fewer PM pieces is the high-speed rotor, while the one with more PM pieces is the low-speed rotor. The high-speed rotor is radially magnetized and the low-speed rotor is tangentially magnetized.

The first and third planes from the left to the right are steady planes, and they formed as one stator component. The PMs on the high-speed rotor are magnetized in the axial direction, while the PMs on the low-speed rotor are magnetized in the circumferential direction. The two rotors are composed of iron and PMs, while the modulator consists of an iron block and non-magnetic parts, which modulate the internal magnetic field. The left auxiliary surface and auxiliary teeth are made of iron with magnetic conductivity. This structure forms a three-layer air gap, with the air gap near the high-speed rotor termed the high-speed rotor air gap, and the air gap near the low-speed rotor referred to as the low-speed rotor air gap. The air gap near the auxiliary teeth is called the auxiliary surface air gap.

For AFS-AMG, its air-gap region has a thin disk shape, and its torque generation method is different from that of RMGs. Hence, to analyze its torque generation mechanism, the AFS-AMG is divided into several slices in the radial direction, and each slice is spread in the circumferential direction on a plane. Hence, the analysis of AFS-AMG can be simplified into analyzing a linear magnetic gear, as depicted in Figure 2.

Since there are a lot of harmonics in AFS-AMG, the magnetic permeance method is adopted for qualitative analysis of a specific slice in the AFS-AMG. First, the magnetomotive force (MMF) of the low-speed rotor's flow and air-gap permeance Λ can be written into Fourier series form:

$$F_{low}(\theta, t) = \sum_{i=1,3,5}^{\infty} F_{low,i} \cos\left(iP_{low}\theta - i\frac{2\pi P_{low}\Omega_{low}}{60}t\right) \quad (1)$$

$$\Lambda(\theta) = \Lambda_0 + \sum_{j=1,3,5}^{\infty} \Lambda_j \cos(jQ_{mod}\theta) \quad (2)$$

where $F_{low,i}$ is the amplitude of the i th harmonic in the MMF; Λ_j is the amplitude of the j th harmonic in the permeance; and P_{low} and Ω_{low} are the pole-pair number and rotating speed of the low-speed rotor, respectively. Q_{mod} is the number of modulator pieces.

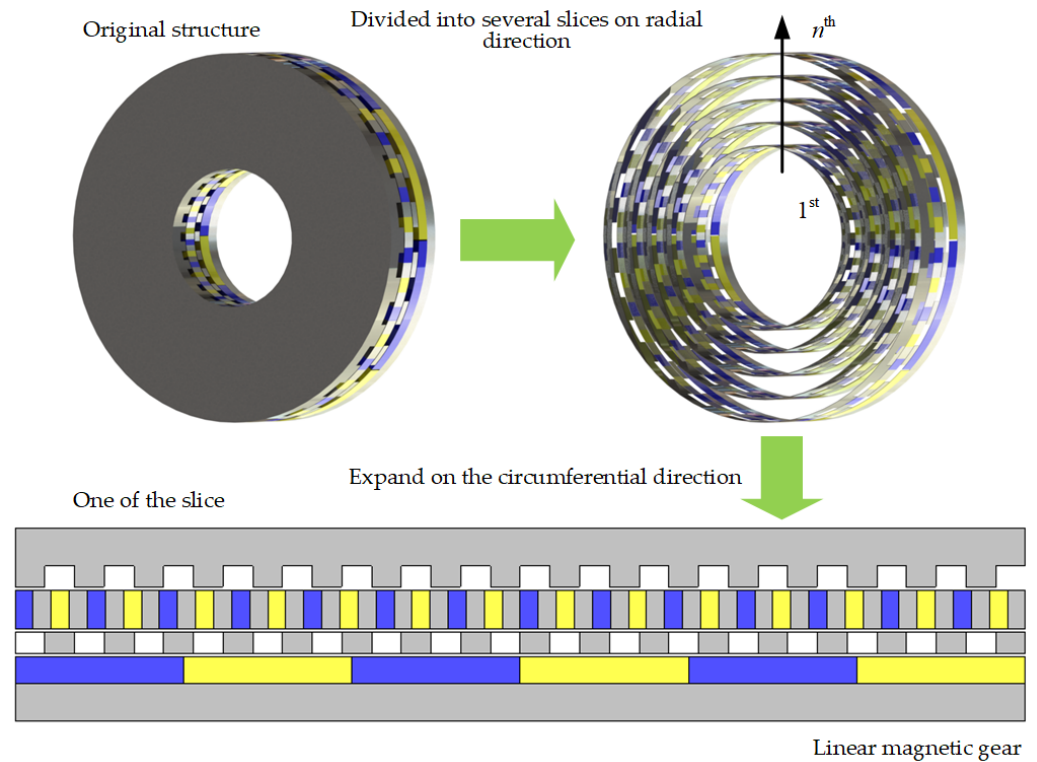


Figure 2. Analysis simplification of the AFS-AMG.

The air-gap magnetic flux ϕ can then be expressed as the product of F and Λ :

$$\begin{aligned}
 \phi_r(\theta, t) &= F_{low}(\theta, t) \cdot \Lambda(\theta) \\
 &= \sum_{i=1,3,5}^{\infty} \Lambda_0 F_{low,i} \cos\left(iP_{low}\theta - i\frac{2\pi P_{low}\Omega_{low}t}{60}\right) \\
 &\quad + \frac{1}{2} F_{low,i} \Lambda_j \cos\left[(iP_{low} + jQ_{mod})\theta - i\frac{2\pi P_{low}\Omega_{low}t}{60}\right] \\
 &\quad + \frac{1}{2} F_{low,i} \Lambda_j \cos\left[(iP_{low} - jQ_{mod})\theta + i\frac{2\pi P_{low}\Omega_{low}t}{60}\right]
 \end{aligned} \tag{3}$$

Then, from the perspective of calculus, magnetic flux density can be regarded as the magnetic flux per unit area. So, the air-gap magnetic flux density B can then be expressed as the product of F and Λ [26,27]:

$$\begin{aligned}
 B_r(\theta, t) &= F_{low}(\theta, t) \cdot \Lambda(\theta) \\
 &= \sum_{i=1,3,5}^{\infty} \Lambda_0 F_{low,i} \cos\left(iP_{low}\theta - i\frac{2\pi P_{low}\Omega_{low}t}{60}\right) \\
 &\quad + \frac{1}{2} F_{low,i} \Lambda_j \cos\left[(iP_{low} + jQ_{mod})\theta - i\frac{2\pi P_{low}\Omega_{low}t}{60}\right] \\
 &\quad + \frac{1}{2} F_{low,i} \Lambda_j \cos\left[(iP_{low} - jQ_{mod})\theta + i\frac{2\pi P_{low}\Omega_{low}t}{60}\right]
 \end{aligned} \tag{4}$$

Due to the modulation effect of the modulator, the order of each harmonic magnetic density contained in the air gap of AMGs can be expressed by the following equation:

$$\begin{aligned}
 p_{n,k} &= |np + kn_m| \\
 n &= 1, 3, 5, \dots, \infty \\
 k &= 0, \pm 1, \pm 2, \pm 3, \dots, \pm \infty
 \end{aligned} \tag{5}$$

where p is the number of magnetic poles of the permanent magnet of the high-speed rotor or low-speed rotor, and n_m is the number of modulation blocks of the modulator. When the modulator is stationary, the rotation speed of the harmonic magnetic density contained in the air-gap magnetic density of the AMG is

$$\Omega_{n,k} = \frac{np}{np + kn_m} \Omega \quad (6)$$

where Ω is the mechanical rotation speed of the high-speed rotor or low-speed rotor. It can be seen from the above equation that the speed of rotation of the space harmonic density is different from the speed of rotation of the rotor carrying the PMs through the modulation of the modulator.

Then, observed from the high-speed rotor side, to produce a steady electromagnetic torque, the pole-pair number of high-speed rotor PMs P_{high} should satisfy [28]

$$P_{high} = |iP_{low} - jQ_{mod}| \quad (7)$$

where i and j should be 1 to maximize the transmitted torque. Therefore, we have

$$P_{high} = Q_{mod} - P_{low} \quad (8)$$

Additionally, since the auxiliary flux-enhancing plane serves as a complementary structure for the magnetic flux to form a shorter loop, its tooth number Q_{teeth} should be equal to the number of modulator pieces, namely,

$$Q_{teeth} = Q_{mod} \quad (9)$$

Next, based on the law of conservation of energy, the rotating speed and output torque relations between the high-speed and low-speed rotor satisfy

$$\frac{T_{high}}{T_{low}} = -\frac{P_{high}}{P_{low}} \quad (10)$$

$$\frac{\Omega_{high}}{\Omega_{low}} = -\frac{P_{low}}{P_{high}} \quad (11)$$

where T_{high} and T_{low} are the electromagnetic torques on the high-speed and low-speed rotor, respectively. Ω_{high} and Ω_{low} are the rotating speeds of the high-speed and low-speed rotor, respectively.

In addition, AFS-AMG's gear ratio G is defined as

$$G = \frac{P_{high}}{P_{low}} \quad (12)$$

2.2. Flux-Enhancing Effect of Extra Modulator

Figure 3 illustrates the magnetic flux density and flux-line distribution on a given slice of the AMG with and without the auxiliary plane simulated in finite element analysis (FEA) software JMAG 22.0. It can be observed that without the auxiliary plane, the magnetic flux path passes through the air region several times to form a closed loop. Since the permeability of air is much lower than that of iron, the magnetic reluctance of the whole loop is very large, leading to a small magnetic flux density in the air gap. However, when the auxiliary plane is added to the outside of the spoke-type PMs, the corresponding flux line changes to pass through a path with smaller reluctance. Hence, the magnetic flux density in the air gap increases, leading to a larger electromagnetic torque.

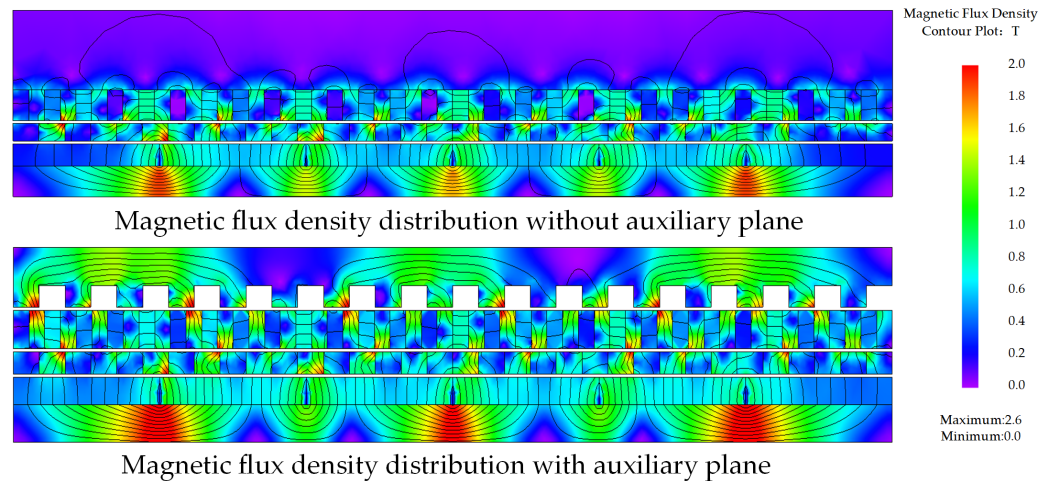


Figure 3. The magnetic flux density distribution of the AFS-AMG with and without the auxiliary plane.

The flux-enhancing effect of the auxiliary plane can also be illustrated by the imaginary flux-line path, as shown in Figure 4. The auxiliary plane acts as a pivotal element in enhancing the magnetic flux within the system, thereby contributing to its overall efficiency and effectiveness. Additionally, the displacement angle between the auxiliary plane and modulator θ_{shift} , as defined in Figure 4, should be equal to zero for maximum torque generation [29].

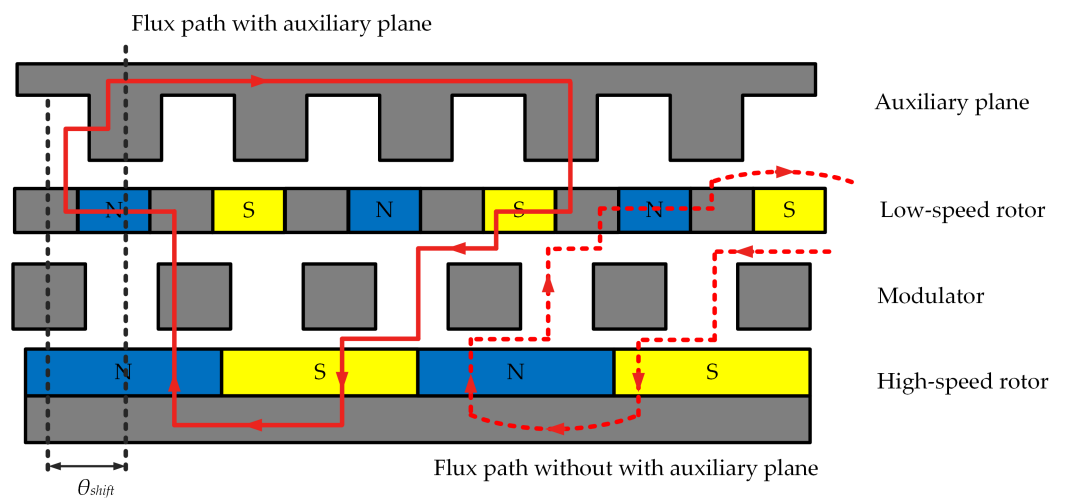


Figure 4. Magnetic flux path illustration of the AFS-AMG with and without the auxiliary plane.

2.3. Evolution of AMGs

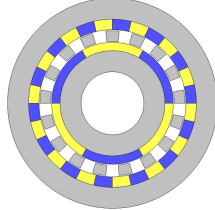
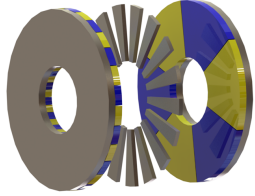
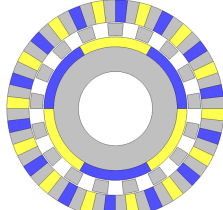
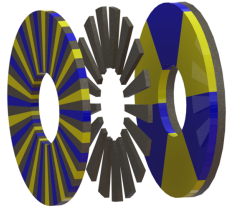
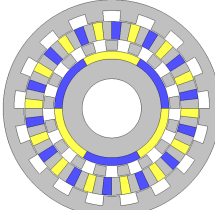
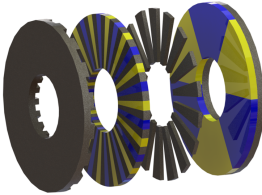
The inherent architectures of axial magnetic gears (AMGs) are fundamentally derived from their radial magnetic gear (RMG) counterparts, as delineated in Table 1 [30]. While the fundamental operational principles of AMGs and RMGs share similarities, their distinctions are primarily manifested in two critical aspects.

First, the orientation of the magnetic flux density significantly diverges between the two gear types. In AMGs, the principal magnetic flux pathways are aligned axially, in contrast to RMGs where these pathways are oriented radially. This axial versus radial flux orientation influences not only the magnetic flux density distribution but also the overall design and operational efficiency of the gears. The axial alignment in AMGs allows for a more uniform flux distribution across the gear width, which is particularly beneficial in applications requiring high torque transmission over compact axial lengths.

Second, the configuration of the rotors in AMGs is arranged axially, which facilitates a multi-plane structural design. This inherent suitability for multi-plane configurations allows for the integration of additional operational layers within the same axial footprint without significantly compromising the gear's compactness. Such a configuration enhances the functional scalability of AMGs and allows them to be particularly efficacious in applications where space is at a premium. Conversely, the incorporation of auxiliary structures such as flux-enhancing planes in RMGs often results in a substantial increase in the gears' overall dimensions. In RMGs, any addition aimed at enhancing magnetic flux typically extends the radial dimension, which can be prohibitive for compact applications.

To further capitalize on the axial configuration, our proposed AFS-AMG integrates auxiliary flux-enhancing structures (AFSs) that are optimally positioned to maximize the impact of magnetic flux enhancement without the typical increase in gear dimensions seen in radial designs. These structures serve to increase the magnetic flux density effectively by channeling and concentrating flux lines through engineered pathways that mitigate leakage and enhance operational efficiency.

Table 1. Mapping relations between RMGs and AMGs.

	RMG	AMG
(a)		
(b)		
(c)		

The evolution of AMG design, as proposed in this paper, incorporates these advanced auxiliary structures by building on the spoke AMG configuration, adding layers of functionality while maintaining a flat, compact structure. It improves the gear's performance in terms of power density and efficiency.

3. Optimization Process

There are two important indexes for the evaluation of AFS-AMGs, namely, the torque density with respect to the total volume τ_{V_total} , and the torque density with respect to the volume of PMs τ_{V_PM} . They can be defined as follows [31]:

$$\tau_{V_total} = \frac{T_{low}}{\pi(R_{out}^2 - R_{in}^2)L} \quad (13)$$

$$\tau_{V-PM} = \frac{T_{low}}{V_{PM}} \quad (14)$$

where R_{in} and R_{out} are the inner and outer radii of the AFS-AMG, respectively. L is the axial length of the AFS-AMG, and V_{PM} is the total volume of PMs in the AFS-AMG.

Given the substantial computational demands of executing a single instance of the AFS-AMG in the FEA software, the application of a genetic-algorithm-based optimization method for AFS-AMGs is time consuming. Consequently, in this work we opt for a parameter sweep method for the optimization process firstly. This approach involves the sequential optimization of the geometrical parameters associated with AFS-AMGs. By methodically altering each parameter within a specified range and evaluating the resulting performance metrics, the optimal configuration can be identified with greater efficiency and less computational expense. Each step in this optimization process is contingent upon the outcomes of the previous steps, ensuring a systematic and coherent development strategy.

3.1. Pole-Pair Combination Selection

To make AMGs with different pole-pair combinations comparable to one another, the gear ratio range is settled at the first stage. Since the gear ratio G should not be an integer to avoid large torque ripple [32,33], its value is set within a range between four and five in this work. Additionally, since iron bars are required to be inserted between each circumferentially magnetized PM, P_{low} should be too large to prevent manufacture difficulties. Hence, the possible pole-pair combinations for AFS-AMGs are listed in Table 2. Figure 5 depicts the electromagnetic torque waveforms on the low-speed rotor of the AFS-AMG with different pole-pair combinations with the same geometrical size. Since the volume of the whole AFS-AMG and PMs do not change with the pole-pair combination variation, it is enough to use T_{low} as the judgment standard. It can be observed that the 4–19 pole-pair combination has the largest torque, and a relatively low torque ripple. Hence, the 4–19 pole-pair combination of AFS-AMGs is chosen for further geometrical parameter optimization.

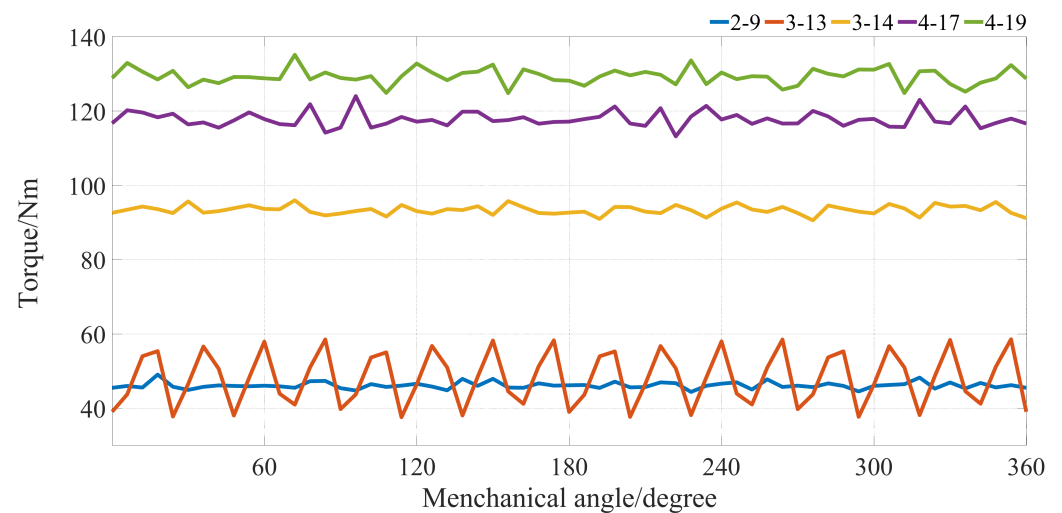


Figure 5. The torque waveforms on the low-speed rotor of AFS-AMGs with different pole-pair combinations.

Table 2. Possible pole-pair combinations of AFS-AMGs.

P_{high}	P_{low}	G
2	9	4.5
3	13, 14	4.33, 4.67
4	17, 19	4.25, 4.75

It is worth noting that while a higher gear ratio generally results in larger torque output in magnetic gears, the efficiency of torque generation is greatly influenced by the number of magnetic poles in the system. Systems with more pole pairs exhibit lower magnetic reluctance, which reduces the stator's opposition to the magnetic field. This minimizes MMF losses, thereby increasing the magnetic flux density and effectively enhancing the torque output. Therefore, although the gear ratio is an important factor, it is not the primary determinant of torque in a magnetic gear system. The internal design and magnetic characteristics of the magnetic rotor, particularly the number of pole pairs, play a crucial role in determining torque capabilities.

3.2. Air-Gap Length Optimization

Another point of concern within the design of AFS-AMG systems pertains to the optimization of the air-gap length, denoted as T_{air} . An excessively large T_{air} significantly elevates the magnetic reluctance, consequently diminishing the torque density of the system. Conversely, a minimal T_{air} complicates the manufacturing process and substantially amplifies the axial force exerted between each plane, potentially compromising structural integrity. To streamline both design and manufacturing processes, the air-gap lengths between the four planes within the AFS-AMG configurations are uniformly established.

As illustrated in Figure 6, the variation in the total tangential torque, τ_{Vtotal} , along with the axial-direction force on the modulator, F_z , as functions of the air-gap length, is presented. Given that the volume of the permanent magnets (PMs) remains constant irrespective of variations in air-gap length, the PM-related torque, τ_{VPM} , is not depicted. The graphical analysis reveals a decline in both τ_{Vtotal} and F_z with the increase in air-gap length. For this study, an air-gap length of 0.6 mm is selected as an optimal compromise, considering factors such as manufacturing precision and the material strength of the modulator in practical engineering applications and the tradeoff between performance and cost. This decision highlights the important balance between achieving high performance and maintaining ease of manufacturing and durability in AFS-AMG system design.

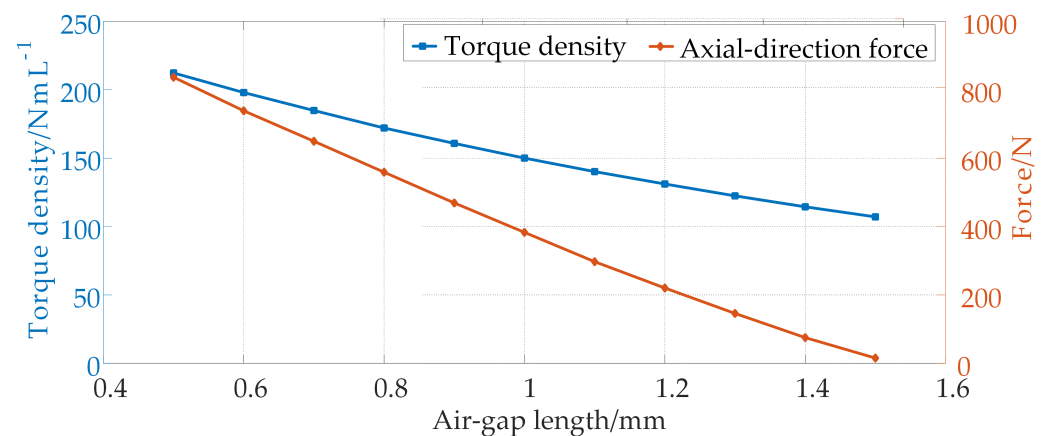


Figure 6. Variation in torque density per volume and axial-direction force on the modulator with respect to air-gap length in AFS-AMGs.

3.3. PM and Modulator Thickness Optimization

The thickness of PMs plays a crucial role in determining the magnitude of the MMF, which, in turn, significantly impacts the magnetic flux density across the air gap, as delineated in Equation (3). Moreover, the thicknesses of the modulator pieces and the auxiliary plane teeth critically influence the extent of magnetic saturation within the silicon steel. This saturation level is a key determinant of the torque density in AFS-AMGs. To streamline the optimization procedure, we propose equalizing the thicknesses of the circumferentially magnetized PMs located on the low-speed rotor and the axially magnetized PMs. This unified thickness parameter is denoted as T_{PM} . Similarly, to facilitate a simplified optimization

framework, the thicknesses of the modulator pieces and the auxiliary plane teeth are also standardized and represented by T_{mod} .

Figure 7 depicts the variations in torque density per volume and torque density per PM volume with respect to T_{PM} and T_{mod} . It can be observed that the variation trends in τ_{Vtotal} and τ_{VPM} are in conflict with one another. For instance, the peak value of τ_{Vtotal} occurs when the value of T_{PM} is 12 mm, but the peak value of τ_{VPM} occurs when the value of T_{PM} is 5 mm. Hence, a trade off must be made to balance the conflict of τ_V total and τ_{VPM} . In this paper, the AFS-AMG with $T_{PM} = 7$ mm, $T_{mod} = 5$ mm is selected, where $\tau_{Vtotal} = 147.1 \text{ Nm}\cdot\text{L}^{-1}$ and $\tau_{VPM} = 781.5 \text{ Nm}\cdot\text{L}^{-1}$.

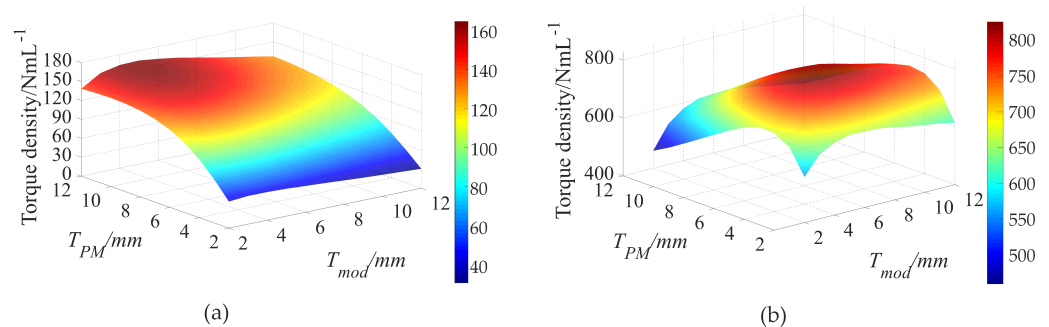


Figure 7. Variation in torque density with respect to the thickness of modulator teeth and PMs: (a) τ_{Vtotal} ; (b) τ_{VPM} .

3.4. Back Iron Thickness Optimization

The thickness of the back iron of the high-speed rotor and auxiliary plane will influence the magnetic saturation, which further affect the electromagnetic torque. To simplify the optimization process, the thickness of the back iron of the high-speed rotor and auxiliary plane are set to be equal, which is represented by T_{iron} . Figure 8 depicts the variations in torque density per volume and torque density per PM volume with respect to T_{iron} . It can be observed that the variation trends in τ_{Vtotal} and τ_{VPM} are in conflict with each other. However, the increasing gradient of becomes smaller when the value of T_{iron} is above 9 mm. Hence, in this paper, T_{iron} is set as 9 mm.

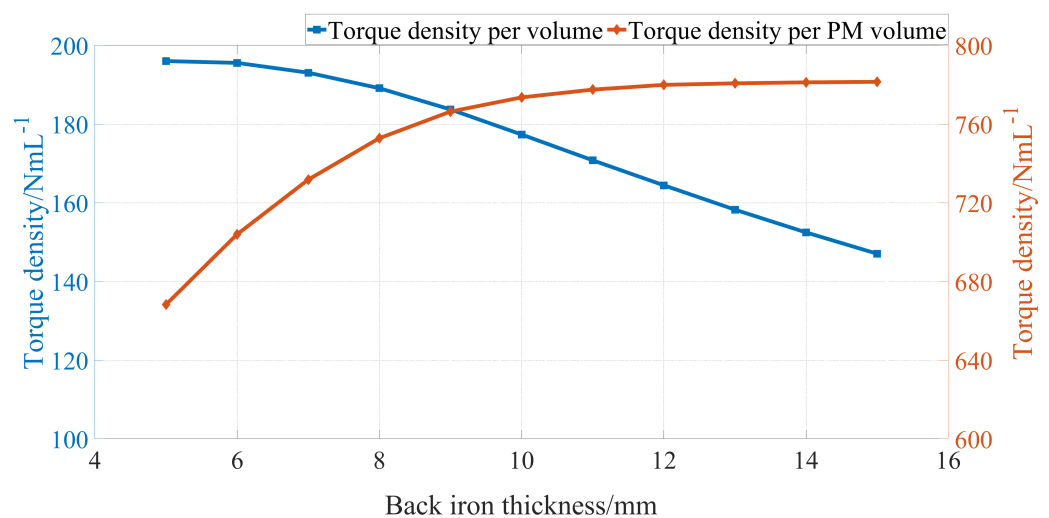


Figure 8. Variation in torque density with respect to the thickness of back iron in AFS-AMGs.

3.5. High-Speed Rotor PM Arc Angle Ratio Optimization

The PMs on the low-speed rotor are adjacent to the silicon steel part, forming a complete plane. If these PMs and silicon steel are not stuck to each other tightly, the

mechanical strength of the low-speed rotor will be affected. However, the PMs on the high-speed rotor are stuck to the back iron, so there could be gaps between each PM block. The arc angle ratio γ of the high-speed rotor PMs is defined as

$$\gamma = \frac{\alpha}{2\pi/P_{high}} \quad (15)$$

Figure 9 depicts the variations in torque density per volume and torque density per PM volume with respect to the arc angle ratio γ . It can be observed that the variation trends in τ_{Vtotal} and τ_{VPM} are in conflict with one another. The decreasing trend in τ_{Vtotal} becomes prominent when γ is above 0.9, while the increasing trend in τ_{VPM} becomes indistinctive when γ is above 0.9. Hence, γ is chosen as 0.9 in this paper.

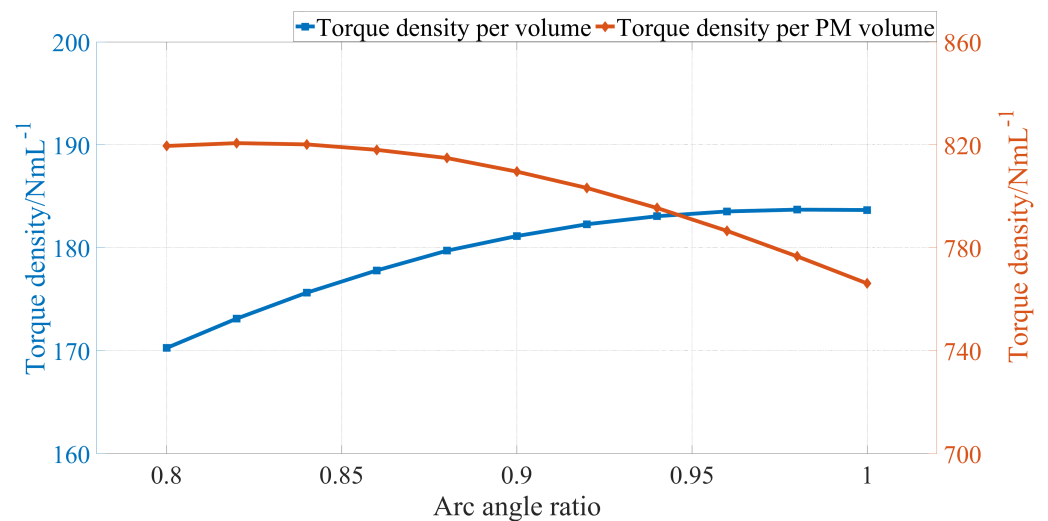


Figure 9. Variation in torque density per PM volume with respect to PMs' arc angle ratio on the high-speed rotor in AFS-AMGs.

3.6. Multi-Objective Optimization

To enhance the design and performance of the axial magnetic gear (AMG), a comprehensive parameter optimization was undertaken using a multi-objective genetic algorithm (MOGA). This approach allows for the simultaneous optimization of multiple parameters, taking into account their complex interdependencies. The variables selected for this optimization, along with their respective ranges, are detailed in Table 3.

Table 3. Parameters of the AMG.

Symbol	Parameter	Initial Value	Range
T_{air}/mm	Air-gap length	0.8	0.5–1.5
T_{PM}/mm	Thickness of PMs on low-speed and high-speed rotors	5	2–12
T_{mod}/mm	Thickness of modulator pieces and auxiliary plane teeth	6	2–12
T_{iron}/mm	Thickness of the back iron of high-speed rotor and auxiliary plane	10	5–15
γ	Arc angle ratio of high-speed rotor PMs	1	0.8–1

The optimization process produced a diverse set of Pareto-optimal solutions, depicted in Figure 10. This Pareto chart demonstrates the feasible trade-offs between minimizing torque ripple and maximizing torque density per unit volume and per unit PM volume. The Pareto-optimal solutions indicated that reductions in torque ripple could be realized with simultaneous increases in torque density per unit volume and per unit PM volume. These improvements highlight the potential for significant enhancements in both the performance and cost efficiency of magnetic gears.

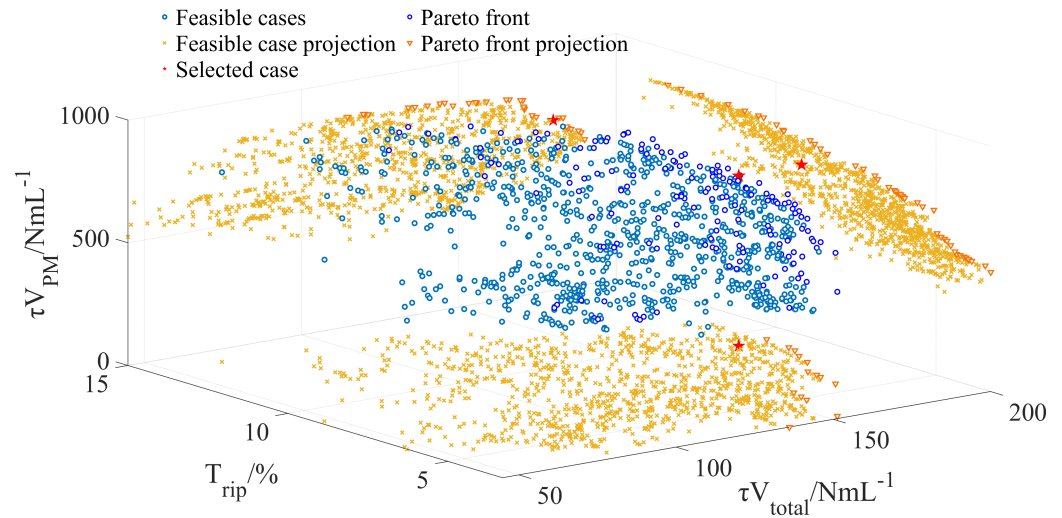


Figure 10. Results of multi-objective optimization.

4. Electromagnetic Performance Evaluation

To prove the superiority of the AFS-AMG, three AMGs with the same inner and outer radii, and similar PM and silicon steel amount were constructed in the FEA software JMAG to compare their performances; their parameters are provided in Table 4. The MG input torque is on the high-speed shaft; therefore, the output power is

$$T_{low}\Omega_{low} = T_{high}\Omega_{high} - P_{loss} \quad (16)$$

where the bracketed torque and power loss terms denote that they are functions of the high-speed rotor input speed Ω_{high} . The loss within the AMG can be separated into:

$$P_{loss} = P_{core} + P_{eddy} \quad (17)$$

where P_{core} is the iron core loss and P_{eddy} is the eddy current loss.

The following formula can be used to calculate the core loss, which includes the eddy current loss and hysteresis loss caused by the laminated structure of electrical steel sheets [34]:

$$P_{core} = \sum \left(\int_V \left(A_e(nf)^2 B_m^2 + A_h(nf) B_m^2 \right) dv \right) \quad (18)$$

where A_e and A_h represent the eddy current loss and hysteresis loss coefficients, respectively. The magnetic flux frequency is denoted by f , and B_m represents the harmonic magnetic flux density.

The calculation of eddy current loss is very important because the generation of eddy current loss can lead to thermal demagnetization. The eddy current loss of a PM can be expressed as the integral of the eddy current density [35]:

$$P_{eddy} = \frac{1}{\sigma} \int J_{eddy} \cdot J_{eddy}^* dV \quad (19)$$

Here, σ represents the conductivity of each material, J_{eddy} represents the eddy current density, and V represents the volume of the material.

The efficiency was calculated by using

$$\text{Efficiency}(\eta) = \frac{P_{out}}{(P_{out} + P_{loss})} \times 100 \quad (20)$$

where P_{out} is the output power and P_{loss} is the power loss.

The corresponding simulation result values are provided in Table 5.

Table 4. Parameters of the AMGs.

Symbol	Parameter	Value
P_{low}	Low-speed rotor PM pole-pairs number	19
P_{high}	High-speed rotor PM pole-pairs number	4
Q	Modulation pieces number	23
R_{out}	Outer radius of the AFS-AMG	80 mm
R_{in}	Inner radius of the AFS-AMG	30 mm
T_{air}	Air-gap length	0.6 mm
T_{PM}	Thickness of PMs on low-speed and high-speed rotors	7 mm
T_{mod}	Thickness of modulator pieces and auxiliary plane teeth	5 mm
T_{iron}	Thickness of the back iron of high-speed rotor and auxiliary plane	9 mm
γ	Arc angle ratio of high-speed rotor PMs	0.9
Ω_{low}	Rotating speed of low-speed rotor	400 r/min
Ω_{high}	Rotating speed of high-speed rotor	1900 r/min

Table 5. Simulation result values of the AMGs.

Symbol	AMG(a)	AMG(b)	AMG(c)
T_{low}/Nm	90.85	98.32	129.65
$\tau_{V_total}/Nm \cdot L^{-1}$	135.51	194.87	171.26
$\tau_{V_PM}/Nm \cdot L^{-1}$	375.56	580.53	712.03
Torque ripple/%	1.28	2.89	8.6
Iron loss/W	27.15	4.53	13.78
PM eddy current loss/W	75.86	17.86	32.51
Efficiency/%	97.36	99.45	99.18

In the study of AMGs, particularly in analyzing their performance metrics, it is essential to consider the iron losses and permanent-magnet (PM) eddy current losses as pivotal factors affecting overall efficiency. Figure 11 compares the performance of the AMGs visually. Among the different configurations examined, AMG(a) exhibits the highest iron and PM eddy current losses, with values reaching 27.15 W and 75.86 W, respectively. In contrast, AMG(c) demonstrates a significant reduction in both iron and PM eddy current losses, recorded at 14.25 W and 31.58 W, respectively, thus offering an improvement over AMG(a). The most efficient configuration in terms of minimizing losses is found in AMG(b), where the iron and PM eddy current losses are identical to those in AMG(c), at 14.25 W and 31.58 W, respectively. When evaluating the overall efficiency, AMG(a) ranks the lowest, with an efficiency of 97.36%. Meanwhile, AMG(c) achieves a higher efficiency of 99.2%, which is only slightly below the efficiency of AMG(b) at 99.45%.

The air-gap density of an AMG contains not only the radial and tangential components, but also the axial component. The axial component of the air-gap density (axial air-gap density) is the most important component of the air-gap density and has the greatest influence on the torque capacity of an AMG. Based on the air-gap density distribution of an axial magnetic gear and using the Maxwell stress tensor method to calculate the torque, the torque and axial force of an AMG can be expressed as

$$T = \frac{(R_o^2 - R_i^2)}{2\mu_0} \int_{R_i}^{R_o} \int_0^{2\pi} B_z(z, r, \theta) B_\theta(z, r, \theta) d\theta dr \quad (21)$$

$$F = \frac{(R_o - R_i)}{2\mu_0} \int_{R_i}^{R_o} \int_0^{2\pi} (B_z^2(z, r, \theta) - B_\theta^2(z, r, \theta)) d\theta dr \quad (22)$$

where μ_0 is the vacuum permeability, and $B_z(z, r, \theta)$ and $B_\theta(z, r, \theta)$ are the axial and tangential components of the air-gap magnetic density at different radii in the axial magnetic

gear, respectively. R_i and R_o are the inner and outer diameters of the axial magnetic gear, respectively.

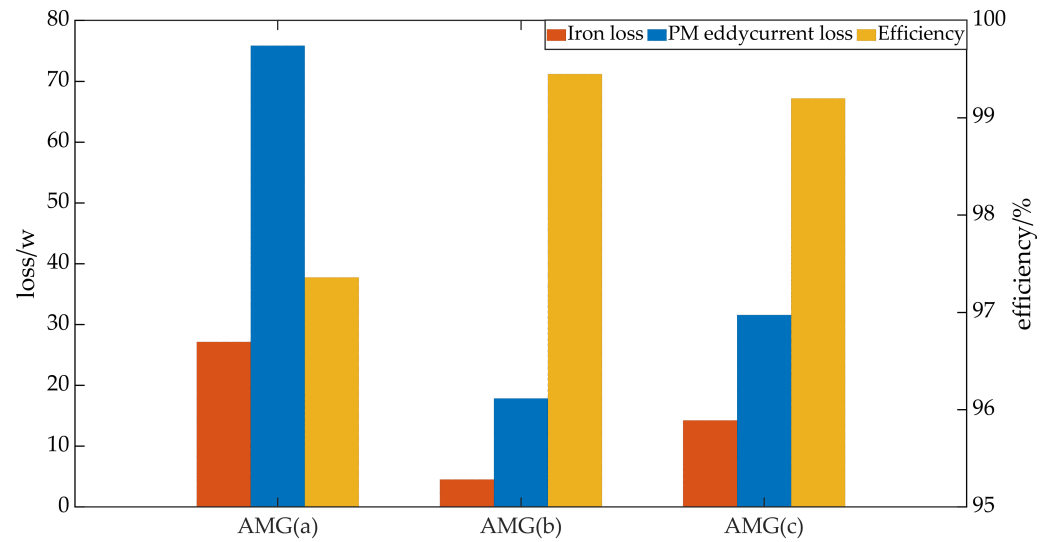


Figure 11. Comparison of the three different AMGs.

Of course, the torque and axial force of the high-speed rotor are only related to the magnetic density distribution in the air gap of the high-speed rotor, and the torque and axial force of the low-speed rotor are only related to the magnetic density distribution in the air gap of the low-speed rotor. Since the air-gap magnetic density at different radii of axial magnetic gears is not the same, in order to simplify the calculation of AMG torque, the air-gap magnetic density at the average radius R_a is used to replace the air-gap magnetic density at different radii, where the calculation formula of the AMG torque and axial force can be converted to

$$T = \frac{(R_o^2 - R_i^2)R_a}{2\mu_0} \int_0^{2\pi} B_z(z, R_a, \theta) B_\theta(z, R_a, \theta) d\theta \quad (23)$$

$$F = \frac{(R_o - R_i)R_a}{2\mu_0} \int_0^{2\pi} (B_z^2(z, R_a, \theta) - B_\theta^2(z, R_a, \theta)) d\theta \quad (24)$$

The axial component $B_z(z, r, \theta)$ and the tangential component $B_\theta(z, r, \theta)$ of the air-gap magnetic density at the mean radius R_m are expressed as follows:

$$B_z(z, R_a, \theta) = \sum_{n=1,2,3}^{+\infty} b_z^n(z, R_a) \cos(n\theta - \varphi_z^n) \quad (25)$$

$$B_\theta(z, R_a, \theta) = \sum_{n=1,2,3}^{+\infty} b_\theta^n(z, R_a) \cos(n\theta - \varphi_\theta^n) \quad (26)$$

where b_z^n and b_θ^n are Fourier coefficients; and φ_z^n and φ_θ^n are the initial angles of the axial and tangential components of each harmonic wave flux density contained in the air-gap flux density at radius R_a , respectively.

So, the calculation formula of the AMG torque can be expressed as

$$T = \frac{\pi(R_o^2 - R_i^2)R_a}{2\mu_0} \sum_{n=1,2,3}^{+\infty} b_z^n(z, R_a) b_\theta^n(z, R_a) \cos(\varphi_z^n - \varphi_\theta^n) \quad (27)$$

$$F = \frac{\pi(R_o - R_i)R_a}{2\mu_0} \sum_{n=1,2,3}^{+\infty} [(b_z^n(z, R_a))^2 - (b_\theta^n(z, R_a))^2] \quad (28)$$

The electromagnetic torque waveforms on the low-speed rotor for the three AMGs are depicted in Figure 12. It can be observed that AFS-AMG(c) has the largest torque density per PM volume. The PM utilization factor of AFS-AMG is 2.15 times that of AMG(a), and 1.40 times that of AMG(b). Additionally, AFS-AMG has a higher efficiency compared with conventional AMGs, namely, AMG(a).

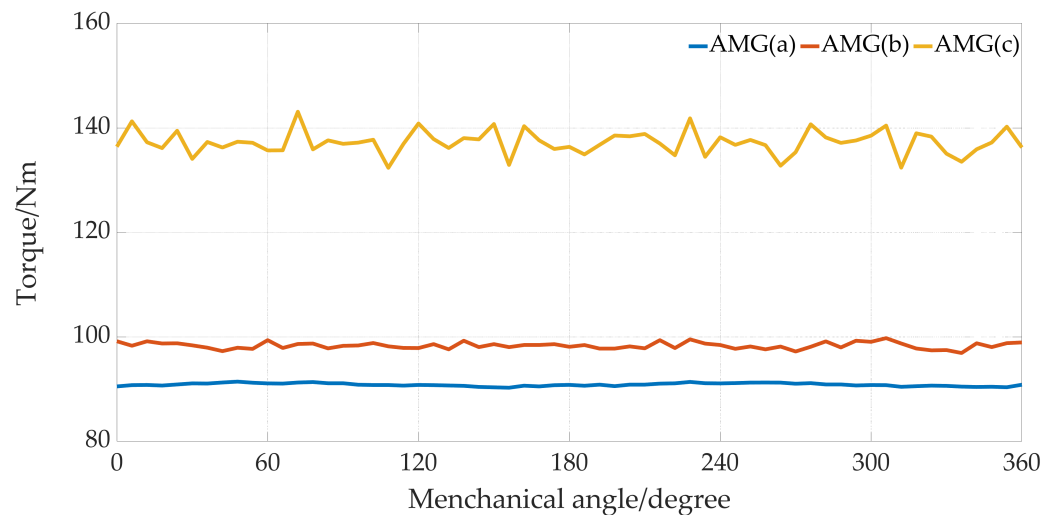
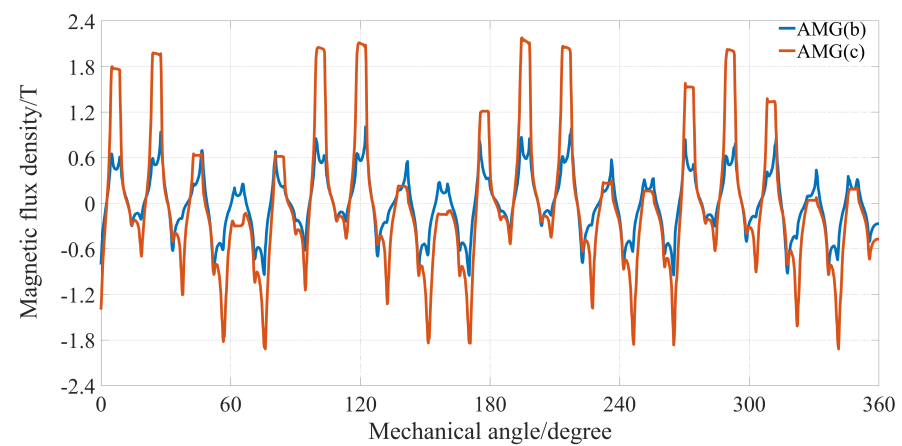


Figure 12. Torque waveforms of the three different AMGs.

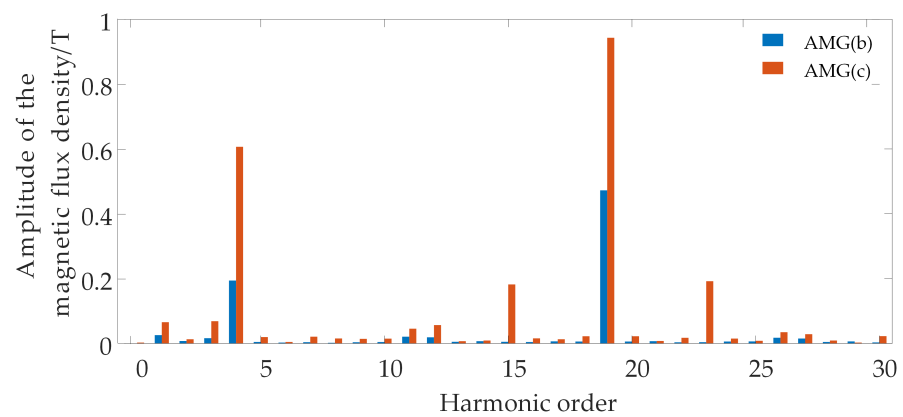
The axial-component magnetic flux density distributions in the air region between the auxiliary plane and the low-speed rotor and the corresponding fast Fourier transform (FFT) of AMG(b) and AMG(c) with radii of 60 mm are depicted in Figure 13. It can be observed that for AMG(c), namely, the AFS-AMG, the amplitudes of working harmonics, namely, the 4th and 19th harmonics, are much larger than those in AMG(b), leading to a torque increase.

The magnetic field distribution of the proposed AMG viewed from the face with fewer PMs and the face with more PMs is shown in Figure 14. It can be observed that the back iron is more easily saturated on the side with fewer PMs, while the auxiliary plane has a lower magnetic field density.

Figure 15 illustrates the axial forces exerted on all components of the AMG, encompassing both the low-speed rotor and the high-speed rotor. Notably, the axial force experienced by the low-speed rotor is relatively significant, reaching 2960 N. Consequently, the axial forces acting on the magnetic steel (N-pole) and the back iron are computed separately for a detailed analysis. Given that the north pole comprises four pieces of magnetic steel, the axial force exerted on each piece is approximately 400 N. This value falls within the tolerance limits of the manufacturing process, indicating its feasibility. In contrast, the average axial force on the high-speed rotor is quantified at around 123 N, a comparatively lower value. The low-speed rotor, due to its reduced speed, completes fewer revolutions per unit of time. Consequently, the frequency of relative motion between the rotor and the modulator is diminished. This infrequency in interaction leads to increased discontinuities in the forces acting on the rotor. Such discontinuities increase the variability in axial force experienced by the low-speed rotor. This is in contrast to the high-speed rotor, where the more frequent interactions due to higher rotational speeds result in a smoother and more continuous force profile, thereby reducing force fluctuations.



(a)



(b)

Figure 13. Magnetic flux density distribution in the circumferential direction with a radius of 60 mm: (a) axial component; (b) the corresponding FFT.

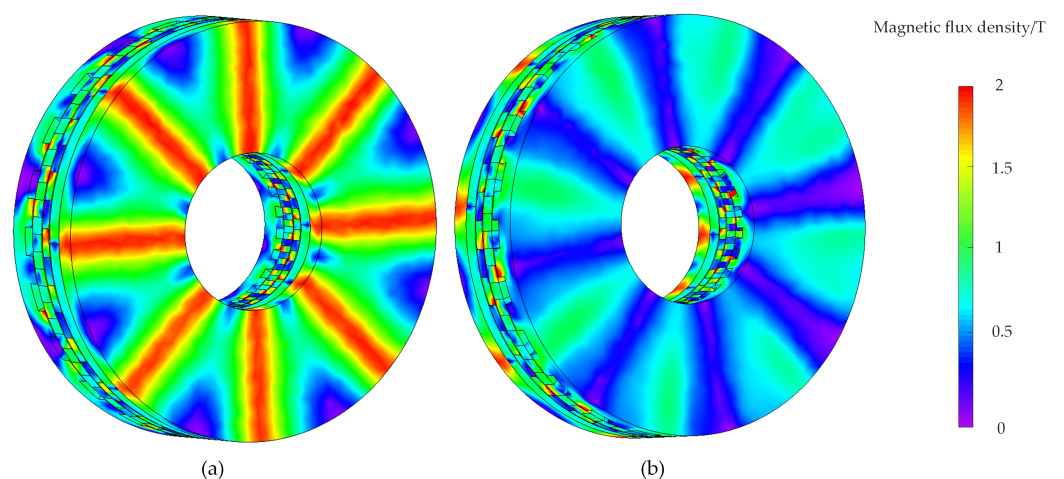


Figure 14. Magnetic field distribution of the proposed AMG: (a) from face with fewer PMs; (b) from face with more PMs.

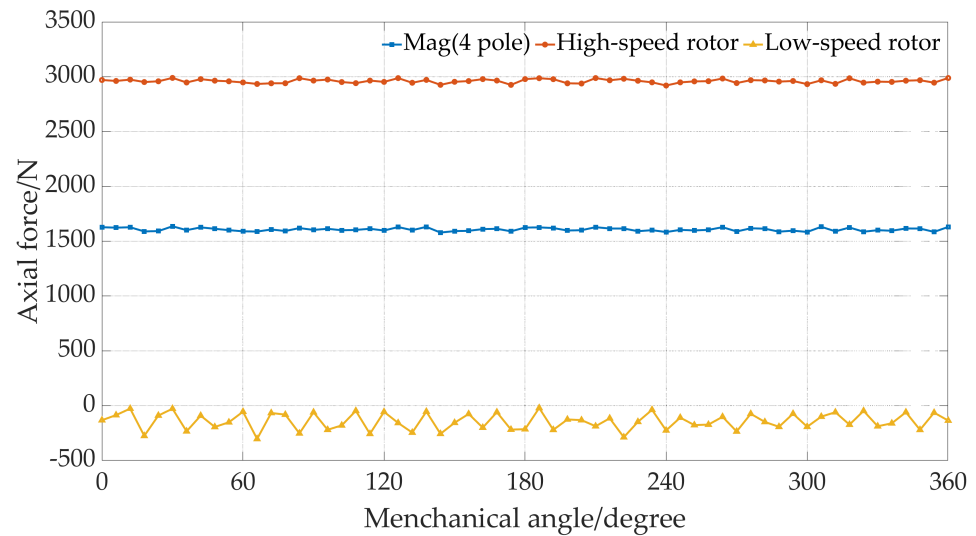


Figure 15. Axial force of the proposed AMG.

The attraction between the two rotors is accompanied by strain on the modular poles. To analyze the results, the stress and strain on the modular poles were calculated using FEA based on Equations (2) and (3).

$$\text{stress}(f) = F/A \quad (29)$$

$$\text{stress}(y) = \delta/L \quad (30)$$

Stress is defined as the force per unit area, where F is the applied force and A is the area. Strain, on the other hand, is the elongation per unit length, where δ is the modified length and L is the existing length. The analysis results are presented in Figure 16, which shows that the stress on the modular pole is $2.218 \times 10^7 \text{ N/m}^2$, a value that is below the yield force ($6.204 \times 10^8 \text{ N/m}^2$) of the material used in the modular pole. The strain is approximately 0.018 mm. The air gap between the modular pole and the two rotors is 0.6 mm. The analysis results indicate that the deformation rate of the magnetic gear is within the allowable range.

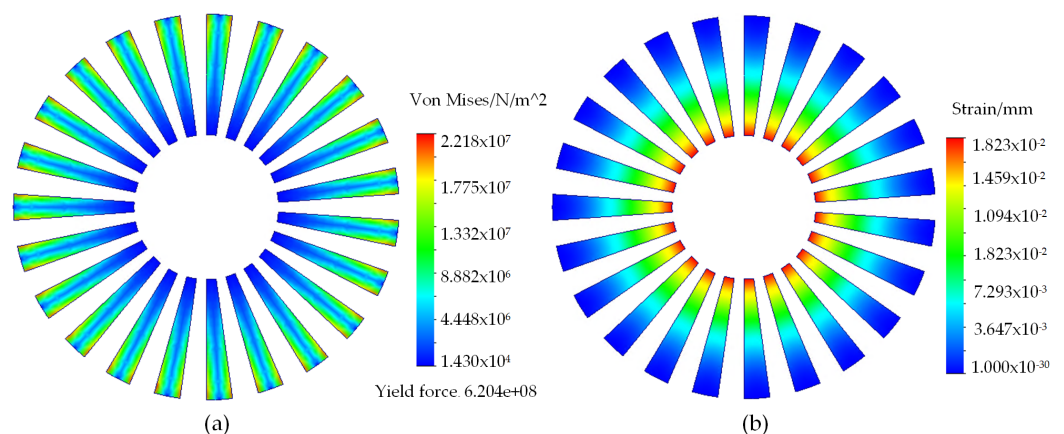


Figure 16. Stress analysis of modulator teeth: (a) stress; (b) strain.

5. Conclusions

In this paper, a novel AFS-AMG is proposed, which has two rotating components: one is composed of axially magnetized PMs, and another one is composed of circumferentially magnetized PMs. Inspired by the structural innovation in RMGs, an auxiliary flux-enhancing slide is introduced in AMGs to decrease the magnetic reluctance in the flux

path; the proposed AFS-AMG has a higher torque density per volume (181.14 Nm/L) and per PM volume (809.6 Nm/L), and a higher efficiency compared to conventional AMG structures. The PM utilization factor of AFS-AMG is twice that of a conventional AMG structure. The simulation results show that the magnetic field distribution of the magnetic gear is reasonable, and the stress on the modulation pole is within a reasonable range.

6. Outlook

Although some aspects of axial magnetic gearing have been investigated in this paper, there are many issues that need to be investigated in greater depth, which can be summarized as the following two areas:

- (1) Prototyping and experimental validation: While simulation results are promising, the next step involves prototyping and rigorous testing under real-world conditions. This will provide invaluable data on the performance, durability, and potential limitations of the AFS-AMG, guiding further refinements.
- (2) Temperature field analysis: This paper does not analyze the temperature field of the AFS-AMG, and further accurate calculation of the temperature field is required. These factors should be comprehensively considered in order to better establish and apply the transmission system of the AFS-AMG.

Author Contributions: Conceptualization, F.L.; methodology, F.L.; software, F.L.; validation, H.Z.; resources, F.L.; data curation, H.Z.; writing—original draft preparation, F.L.; writing—review and editing, F.L.; visualization, X.S.; supervision, H.Z.; project administration, H.Z.; funding acquisition, H.Z. All authors have read and agreed to the published version of the manuscript.

Funding: This work was supported in part by the Guangdong Basic and Applied Basic Research Foundation under Project 2022A1515110361, University Innovation Project in Guangdong Province Supported by Guangdong Provincial Department of Education Project 2023KTSCX172 and Guangzhou-HKUST(GZ) Joint Funding Program 2024A03J0618.

Institutional Review Board Statement: Not applicable.

Informed Consent Statement: Not applicable.

Data Availability Statement: Data are contained within the article.

Conflicts of Interest: The authors declare no conflicts of interest.

References

1. Li, K.; Bird, J.Z. A review of the volumetric torque density of rotary magnetic gear designs. In Proceedings of the 2018 XIII International Conference on Electrical Machines (ICEM), Alexandroupoli, Greece, 3–6 September 2018; pp. 2016–2022.
2. Ribrant, J.; Bertling, L. Survey of failures in wind power systems with focus on Swedish wind power plants during 1997–2005. In Proceedings of the 2007 IEEE Power Engineering Society General Meeting, Tampa, FL, USA, 24–28 June 2007; pp. 1–8.
3. Zhao, H.; Liu, C.; Song, Z.; Yu, J. A fast optimization scheme of coaxial magnetic gears based on exact analytical model considering magnetic saturation. *IEEE Trans. Ind. Appl.* **2020**, *57*, 437–447. [[CrossRef](#)]
4. Rasmussen, P.O.; Andersen, T.O.; Jorgensen, F.T.; Nielsen, O. Development of a high-performance magnetic gear. *IEEE Trans. Ind. Appl.* **2005**, *41*, 764–770. [[CrossRef](#)]
5. Jing, L.; Liu, W.; Tang, W.; Qu, R. Design and Optimization of Coaxial Magnetic Gear With Double-Layer PMs and Spoke Structure for Tidal Power Generation. *IEEE/ASME Trans. Mechatron.* **2023**, *28*, 3263–3271. [[CrossRef](#)]
6. Aloeyi, E.F.; Shoaei, A.; Wang, Q. A hybrid coaxial magnetic gear using flux-focusing halbach permanent magnet arrangement. In Proceedings of the 2023 IEEE 14th International Conference on Power Electronics and Drive Systems (PEDS), Montreal, QC, Canada, 7–10 August 2023; pp. 1–6.
7. Zhao, H.; Liu, C.; Dong, Z.; Huang, R.; Li, X. Design and optimization of a magnetic-gear direct-drive machine with V-shaped permanent magnets for ship propulsion. *IEEE Trans. Transp. Electr.* **2021**, *8*, 1619–1633. [[CrossRef](#)]
8. Li, X.; Wei, Z.; Zhao, Y.; Wang, X.; Hua, W. Design and analysis of surface-mounted permanent-magnet field-modulation machine for achieving high power factor. *IEEE Trans. Ind. Electron.* **2024**, *71*, 4375–4386. [[CrossRef](#)]
9. Aiso, K.; Akatsu, K.; Aoyama, Y. A novel reluctance magnetic gear for high-speed motor. *IEEE Trans. Ind. Appl.* **2019**, *55*, 2690–2699. [[CrossRef](#)]

10. Jørgensen, F.T.; Andersen, T.O.; Rasmussen, P.O. The cycloid permanent magnetic gear. In Proceedings of the Conference Record of the 2006 IEEE Industry Applications Conference Forty-First IAS Annual Meeting, Tampa, FL, USA, 8–12 October 2006; Volume 1; pp. 373–378.
11. Huang, C.C.; Tsai, M.C.; Dorrell, D.G.; Lin, B.J. Development of a magnetic planetary gearbox. *IEEE Trans. Magn.* **2008**, *44*, 403–412. [[CrossRef](#)]
12. Atallah, K.; Wang, J.; Howe, D. A high-performance linear magnetic gear. *J. Appl. Phys.* **2005**, *97*, 10N516. [[CrossRef](#)]
13. Pakdelian, S.; Frank, N.W.; Toliyat, H.A. Magnetic design aspects of the trans-rotary magnetic gear. *IEEE Trans. Energy Convers.* **2014**, *30*, 41–50. [[CrossRef](#)]
14. Chen, Y.; Fu, W.N.; Ho, S.L.; Liu, H. A quantitative comparison analysis of radial-flux, transverse-flux, and axial-flux magnetic gears. *IEEE Trans. Magn.* **2014**, *50*, 1–4. [[CrossRef](#)]
15. Tsurumoto, K.; Kikuchi, S. A new magnetic gear using permanent magnet. *IEEE Trans. Magn.* **1987**, *23*, 3622–3624. [[CrossRef](#)]
16. Tsurumoto, K. Power transmission of magnetic gear using common meshing and insensibility to center distance. *IEEE Transl. J. Magn. Japan* **1988**, *3*, 588–589. [[CrossRef](#)]
17. Tsurumoto, K. Some considerations on the improvement of performance characteristics of magnetic gear. *IEEE Transl. J. Magn. Japan* **1989**, *4*, 576–582. [[CrossRef](#)]
18. Kläui, E. Electrodynamic Transmission and a Centrifugal Pump with a Transmission of This Kind. U.S. Patent 6,217,298, 17 April 2001.
19. Meisberger, A. Magnetic Gear and Centrifuge Having a Magnetic Gear. U.S. Patent 6,440,055, 27 August 2002.
20. Zhu, D.; Yang, F.; Du, Y.; Xiao, F.; Ling, Z. An axial-field flux-modulated magnetic gear. *IEEE Trans. Appl. Supercond.* **2016**, *26*, 1–5. [[CrossRef](#)]
21. Acharya, V.M.; Bird, J.Z.; Calvin, M. A flux focusing axial magnetic gear. *IEEE Trans. Magn.* **2013**, *49*, 4092–4095. [[CrossRef](#)]
22. Kouhshahi, M.B.; Bird, J.Z.; Acharya, V.M.; Li, K.; Calvin, M.; Williams, W.; Modaresahmadi, S. An axial flux focusing magnetically geared generator for low input speed applications. *IEEE Trans. Ind. Appl.* **2019**, *56*, 138–147. [[CrossRef](#)]
23. Hu, F.; Zhou, Y.; Cui, H.; Liu, X. Spectrum analysis and optimization of the axial magnetic gear with Halbach permanent magnet arrays. *Energies* **2019**, *12*, 2003. [[CrossRef](#)]
24. Afsari, S. Optimal design and analysis of a novel reluctance axial flux magnetic gear. *Sci. Iran.* **2022**, *29*, 1573–1580. [[CrossRef](#)]
25. Afsari, S.A.; Heydari, H.; Dianati, B. Cogging torque mitigation in axial flux magnetic gear system based on skew effects using an improved quasi 3-D analytical method. *IEEE Trans. Magn.* **2015**, *51*, 1–11. [[CrossRef](#)]
26. Cheng, M.; Han, P.; Hua, W. General airgap field modulation theory for electrical machines. *IEEE Trans. Ind. Electron.* **2017**, *64*, 6063–6074. [[CrossRef](#)]
27. Zhu, Z.Q.; Liu, Y. Analysis of air-gap field modulation and magnetic gearing effect in fractional-slot concentrated-winding permanent-magnet synchronous machines. *IEEE Trans. Ind. Electron.* **2017**, *65*, 3688–3698. [[CrossRef](#)]
28. Atallah, K.; Howe, D. A novel high-performance magnetic gear. *IEEE Trans. Magn.* **2001**, *37*, 2844–2846. [[CrossRef](#)]
29. Zhao, H.; Liu, C.; Song, Z.; Wang, W.; Lubin, T. A dual-modulator magnetic-geared machine for tidal-power generation. *IEEE Trans. Magn.* **2020**, *56*, 1–7. [[CrossRef](#)]
30. Zhang, X.; Liu, X.; Chen, Z. A novel dual-flux-modulator coaxial magnetic gear for high torque capability. *IEEE Trans. Energy Convers.* **2017**, *33*, 682–691. [[CrossRef](#)]
31. Gardner, M.C.; Johnson, M.; Toliyat, H.A. Comparison of surface permanent magnet coaxial and cycloidal radial flux magnetic gears. In Proceedings of the 2018 IEEE Energy Conversion Congress and Exposition (ECCE), Portland, OR, USA, 23–27 September 2018; pp. 5005–5012.
32. Praslicka, B.; Gardner, M.C.; Johnson, M.; Toliyat, H.A. Review and analysis of coaxial magnetic gear pole pair count selection effects. *IEEE J. Emerg. Sel. Top. Power Electron.* **2021**, *10*, 1813–1822. [[CrossRef](#)]
33. Nielsen, S.S.; Wong, H.Y.; Baninajar, H.; Bird, J.Z.; Rasmussen, P.O. Pole and segment combination in concentric magnetic gears: Vibrations and acoustic signature. *IEEE Trans. Energy Convers.* **2022**, *37*, 1644–1654. [[CrossRef](#)]
34. Tian, Y.; Liu, G.; Zhao, W.; Ji, J. Design and analysis of coaxial magnetic gears considering rotor losses. *IEEE Trans. Magn.* **2015**, *51*, 1–4. [[CrossRef](#)]
35. Chen, Q.; Liang, D.; Jia, S.; Wan, X. Analysis of multi-phase and multi-layer fractional-slot concentrated-winding on PM eddy current loss considering axial segmentation and load operation. *IEEE Trans. Magn.* **2018**, *54*, 1–6. [[CrossRef](#)]

Disclaimer/Publisher’s Note: The statements, opinions and data contained in all publications are solely those of the individual author(s) and contributor(s) and not of MDPI and/or the editor(s). MDPI and/or the editor(s) disclaim responsibility for any injury to people or property resulting from any ideas, methods, instructions or products referred to in the content.